PHYSICAL REVIEW C **104**, 015806 (2021)

Editors' Suggestion

Stellar *s*-process neutron capture cross sections on ^{78,80,84,86}Kr determined via activation, atom trap trace analysis, and decay counting

M. Tessler,[1,2] J. Zappala,[3] S. Cristallo,[4,5] L. Roberti,[6,7] M. Paul,[2,*] S. Halfon,[1] T. Heftrich,[8] W. Jiang,[9] D. Kijel,[1]
A. Kreisel,[1] M. Limongi,[6,5,10] Z.-T. Lu,[9] P. Müller,[3] R. Purtschert,[11] R. Reifarth,[8] A. Shor,[1] D. Veltum,[8] D. Vescovi,[12,5,4]
M. Weigand,[8] and L. Weissman[1]
[1]*Soreq Nuclear Research Center, Yavne 81800, Israel*
[2]*Racah Institute of Physics, Hebrew University, Jerusalem 91904, Israel*
[3]*Argonne National Laboratory, Argonne, Illinois 60439, USA*
[4]*INAF - Osservatorio Astronomico d'Abruzzo, via Maggini snc, Teramo, Italy*
[5]*INFN - Sezione di Perugia, via A. Pascoli, Perugia, Italy*
[6]*INAF - Osservatorio Astronomico di Roma, via Frascati 33, Monte Porzio Catone, Italy*
[7]*Dipartimento di Fisica, "Sapienza" Universit di Roma, Piazzale Aldo Moro 5, 00185 Rome, Italy*
[8]*Goethe University Frankfurt, Frankfurt 60438, Germany*
[9]*Hefei National Laboratory for Physical Sciences at the Microscale, CAS Center for Excellence in Quantum Information and Quantum Physics, University of Science and Technology of China, 96 Jinzhai Road, Hefei 230026, China*
[10]*Kavli Institute for the Physics and Mathematics of the Universe (Kavli IPMU, WPI), Todai Institutes for Advanced Study, The University of Tokyo, Kashiwa 277-8583, Japan*
[11]*Physics Institute, University of Bern, 3012 Berne, Switzerland*
[12]*Gran Sasso Science Institute, Viale Francesco Crispi, 7, L'Aquila, Italy*

(Received 29 December 2020; accepted 29 April 2021; published 29 July 2021)

We present a detailed account of neutron capture experiments of astrophysical relevance on $^{78,80,84,86}\mathrm{Kr}(n,\gamma)$ reactions at the border between weak and main *s* process. The experiments were performed with quasi-Maxwellian neutrons from the Liquid-Lithium Target (LiLiT) and the mA-proton beam at 1.93 MeV (2–3 kW) of the Soreq Applied Research Accelerator Facility (SARAF). The setup yields high-intensity ≈40 keV quasi-Maxwellian neutrons (3–5 $\times 10^{10}$ n/s) closely reproducing the conditions of *s*-process stellar nucleosynthesis. A sample of 100 mg of atmospheric, pre-nuclear-age Kr gas contained in a Ti spherical shell was activated in the LiLiT neutron field. The abundances of long-lived Kr isotopes (^{81,85g}Kr) were measured by atom counting via atom trap trace analysis (ATTA) at Argonne National Laboratory and low-level counting (LLC) at University of Bern. This work is the first measurement of a nuclear cross section using atom counting via ATTA. The activities of short-lived Kr isotopes (^{79,85m,87}Kr) were measured by γ-decay counting with a high-purity germanium detector. Maxwellian-averaged cross sections for *s*-process thermal energies are extracted. By comparison to reference values, our nucleosynthesis network calculations show that the experimental cross sections have a strong impact on calculated abundances of krypton and neighboring nuclides, in some cases improving agreement between theory and observations.

DOI: 10.1103/PhysRevC.104.015806

I. INTRODUCTION

Stellar synthesis of heavy nuclides ($A \gtrsim 56$) proceeds in major part via neutron captures and is traditionally divided, since the seminal papers of Cameron [1] and Burbidge *et al.* [2], into a slow (s) process and a rapid (r) process. The s process, which evolves by successive captures and decays close to the valley of stability, has been extensively studied both experimentally and theoretically (see [3–5]). The krypton stable isotopes are of special interest in several regards as follows. They reside in a region of nuclides (Fig. 1) sensitive to two types of s processes, coined *weak* ($56 \lesssim A \lesssim 90$) and *main* ($A \gtrsim 90$), attributed respectively to the evolution of massive and low-mass stars. The heavier stable isotopes ^{84,86}Kr are also subject to a substantial contribution from the r process (see [6] for a recent estimate). On the other hand, two of its lighter isotopes, ^{80,82}Kr, shielded from the r process by ^{80,82}Se, are pure s-process nuclides making their natural abundances [7–9] solid anchors for the validation of s-process models (see [6] and references therein). The determination of Kr solar abundances via analysis of primitive meteorites (C1 carbonaceous chondrites) is, however, difficult, and Kr isotopic composition in meteorites is considered a prominent anomalous case in the s-process pattern [10,11]. The few Kr measurements on acid residues of SiC presolar grains [12] have been theoretically interpreted as a mix between solar material and nucleosynthesis products of asymptotic giant branch (AGB) stars [13].

---

[*] Corresponding author: paul@vms.huji.ac.il

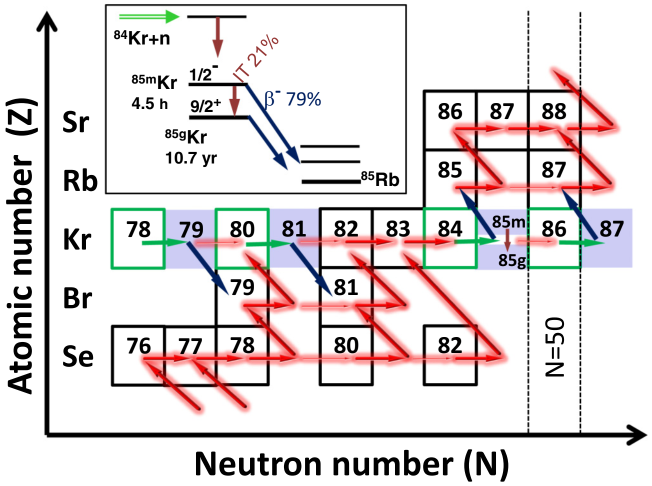

FIG. 1. The *s*-process path in the krypton region (thick arrows indicate the primary *s*-process flow, shaded lines indicate weaker captures). Green (solid horizontal arrows) mark the neutron capture reactions studied in this work by activation, while blue (diagonal) arrows identify β decays. A zoom of the branching at ^{85}Kr, including β decays and internal transitions, is highlighted.

The ^{84}Kr(n,γ) reaction is especially interesting: the ^{85}Kr neutron capture product behaves as a branching point of the *s* process [5] owing to a ground state ^{85g}Kr of half-life 10.7 yr comparable to the mean time between neutron captures during the convective shell episodes characterizing the thermally pulsing (TP) AGB phase of a low or intermediate mass star. Owing to the level scheme of ^{85}Kr, this half-life is unchanged from its laboratory value under stellar conditions and the branching point is one from which the neutron density of the *s*-process site can practically be derived. The first excited state (see Fig. 1 inlet), an isomeric state ^{85m}Kr at 304.9 keV excitation energy, of much shorter half-life (4.48 h), decays partly (21.2%) by isomeric transition (IT) to the ground state but also diverts a major part of its own production (78.8%) towards ^{85}Rb by direct β^- decay. The low spin of ^{85m}Kr $(1/2^-)$ enhances its population relative to that of the ground state ^{85g}Kr $(9/2^-)$, and the isomeric short-lived population, not thermally equilibrated before β decay, becomes a sensitive probe of high neutron densities. Finally, the study of ^{86}Kr is of particular interest, because it has a neutron magic number ($N = 50$); as a matter of fact, this isotope may act as a bottleneck for the *s* process due to its particularly stable configuration against neutron captures.

The understanding of the *s*-process impact on the Kr isotope abundances requires reliable neutron capture cross sections both for stable and unstable nuclides in *s*-process conditions. Some of these were measured [14–20] with various degrees of mutual agreement; see also [21] for an experimental determination of the ^{85}Kr$(n,\gamma)^{86}$Kr reaction via its inverse ^{86}Kr$(\gamma,n)^{85}$Kr reaction. The objective of the present work was a measurement of (n,γ) reactions on all stable Kr isotopes that can be studied by the activation technique. We measured the ^{78,80,84,86}Kr(n,γ) reaction cross sections by activation with quasi-Maxwellian neutrons produced by the ^{7}Li(p,n) reaction at the superconducting Soreq Applied Research Accelerator Facility (SARAF) [22,23] using the Liquid-Lithium Target (LiLiT) [24,25]. The activities of the short-lived Kr isotopes (^{79,85m,87}Kr) were measured by decay counting via γ spectrometry. The long-lived Kr isotopes (^{81,85g}Kr) were measured by atom counting via atom trap trace analysis (ATTA) at the TRACER Center of Argonne National Laboratory (ANL) and low-level counting (LLC) at University of Bern. Preliminary results of these experiments were reported in [26].

II. EXPERIMENTAL METHOD A: ACTIVATION OF Kr SAMPLES

In order to determine the Maxwellian Average Cross Section (MACS),

$$\mathrm{MACS}(kT) = \frac{2}{\sqrt{\pi}} \frac{\int_0^\infty \sigma(E_n) E_n e^{-\frac{E_n}{kT}} dE_n}{\int_0^\infty E_n e^{-\frac{E_n}{kT}} dE_n} \tag{1}$$

relevant to an astrophysical site, a neutron source coined quasi-Maxwellian, emitting neutrons with an energy distribution $dn/dE \approx Ee^{-\frac{E}{E_0}}$, is used to activate a sample, where E_0 plays the role of an effective thermal energy kT. The endothermic ($Q = -1.644$ MeV) reaction ^{7}Li$(p,n)^7$Be has been extensively studied experimentally since the 1940s [27,28] and is a well-known neutron source in the keV region. Taking advantage of the kinematic properties of the ^{7}Li$(p,n)^7$Be reaction, it was shown in particular that for an incident proton energy ≈ 30 keV above the reaction threshold ($E_{th} = 1880.4$ keV) on a thick Li target, the neutrons are emitted in a forward cone of $\approx \pm 60^\circ$ angular opening with an energy distribution similar to that of a Maxwell-Boltzmann (MB) flux with $kT \approx 30$ keV [29,30]. Activation of a secondary target in this quasi-Maxwellian neutron field mimics the stellar *s*-process capture in the laboratory.

An intense ^{7}Li$(p,n)^7$Be neutron source based on the Liquid-Lithium Target (LiLiT) [23–25], developed and built at SARAF, is used for MACS measurements. The SARAF accelerator is based on a continuous wave (CW), proton/deuteron RF superconducting linear accelerator, capable of delivering currents up to 2 mA. Phase I of SARAF, operational between 2013 and 2019, produced proton and deuteron beams with energies up to ≈4 and 5 MeV respectively [22,31]. Phase I consisted of a 20 keV/u electron cyclotron resonance (ECR) ion source injector, a low-energy beam transport section (LEBT), a four-rod radio frequency quadrupole (1.5 MeV/u), a medium energy beam transport section, a prototype superconducting module housing six half-wave resonators and three superconducting solenoids and a diagnostic plate (D-plate). The beamline downstream from the accelerator, transported the high-intensity beam to the target position, in this case to LiLiT. Phase II of SARAF, currently under construction, will be capable of delivering deuteron (proton) beams up to 40 (35) MeV at currents up to 5 mA.

The SARAF high intensity beam requires a Li target that can withstand its beam power, incompatible with targets of solid Li or Li compounds due to their poor thermal properties. LiLiT [23–25,32] consists of a loop of circulating liquid

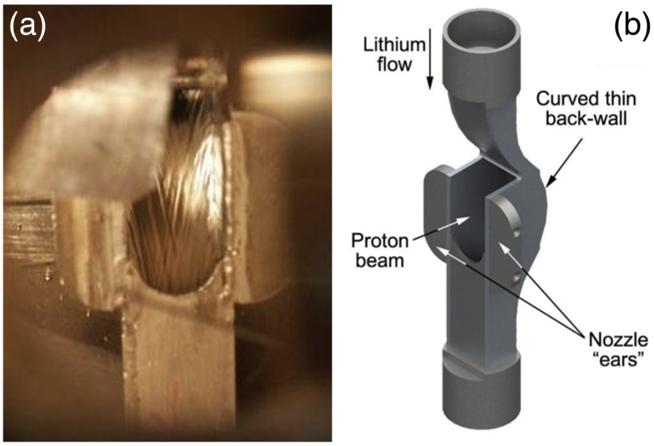

FIG. 2. (a) The 18 mm wide, 1.5 mm thick lithium film, as photographed through the vacuum chamber view port, flows on the concave back wall of the lithium nozzle. A tantalum plate used for beam positioning can be seen near the upper left corner of the lithium nozzle. When extracted, the plate clears the beam path. (b) Drawing of the nozzle and open duct. The holes in the sides of the nozzle "ears" are used for inserting thermocouple wires for temperature readings.

lithium at ≈200 °C. A 1.5 mm thick film of liquid lithium is forced-flown at high velocity (2–5 m/s) through a nozzle onto a concave-curvature open duct improving the hydrodynamical stability of the flow; the back wall of the duct is made of 0.5 mm stainless steel (Fig. 2). The target is bombarded by the high-intensity proton beam impinging directly on the windowless Li-vacuum interface. The first few microns at the surface of the liquid-lithium film serve as the neutron-producing thick target and the deeper layers as a beam dump, from which the power is transported by the flow to a heat exchanger. A 25 cm diameter 0.5 mm thick stainless steel wall shaped as a spherical cap is located ≈ 1 mm beyond the curved duct and seals the LiLiT (and beam pipe) vacuum. This wall's curvature is opposite to that of the duct, enabling sample positioning behind the curved wall close to the neutron source in a separately evacuated experimental chamber [23,24] (Fig. 3).

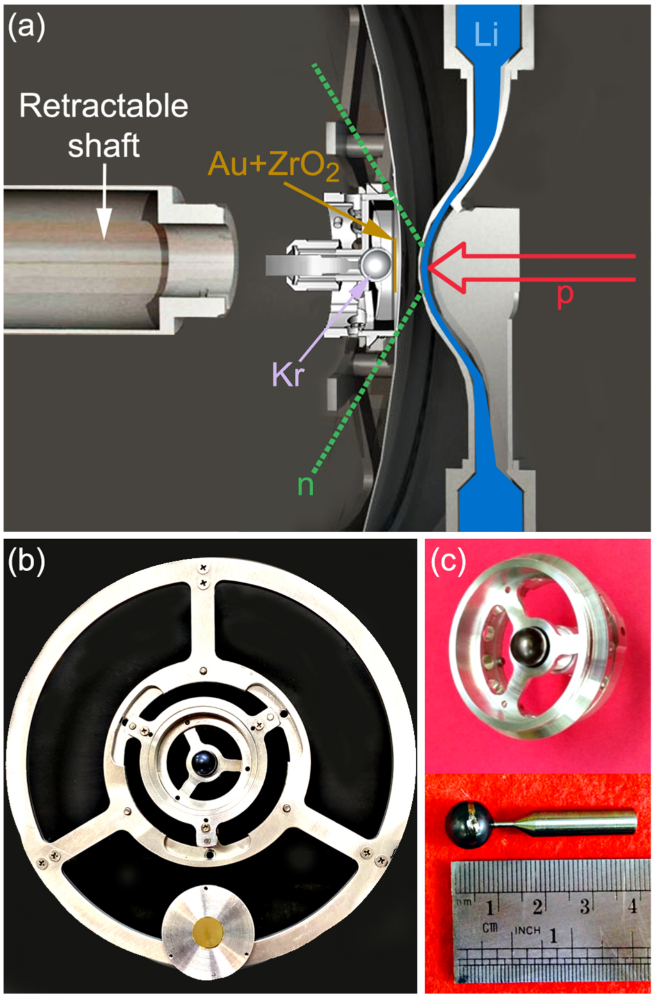

FIG. 3. (a) Diagram of the Liquid-Lithium Target (LiLiT) and activation target assembly. The (≈1.5 mA, ≈ 9 mm full width) proton beam (open red arrow) impinges on the free-surface lithium film (blue) (see [24] for details). The Kr-filled sphere (see text) and Au foil are positioned in the outgoing neutron cone (green dotted lines) in a vacuum chamber separated from the LiLiT chamber. The retractable shaft (at left) is used to load and unload rapidly the target assembly. (b) Photograph of the Kr gas sphere mounted in an aluminum circular frame on the center line of the chamber. A 0.5 mm thick pure Al plate (displaced for clarity to the bottom of the figure to unveil the sphere) supports the Au monitor and a thin (parasitic) ZrO$_2$ target, covering the Kr-filled sphere. (c) Ti sphere (see [33] for details) used to contain the pressurized Kr gas for irradiation and the sphere holder for irradiation at SARAF-LiLiT.

The proton beam energy (1930 ± 5 keV) was measured in pulse mode by time of flight and by Rutherford backscattering spectrometry at the D-plate using a thin gold foil that can be inserted into the halo of the intense proton beam [34]. The energy spread, characteristic of RF linacs, was measured by a threshold curve for the ^{7}Li(p, n) reaction which has an energy threshold $E_p = 1880.4$ keV. The energy spread was also measured via an energy scan on a ^{13}C target around the ^{13}C(p, γ) resonance at 1747 keV. See [34] for more details of these measurements. The two techniques determined a proton energy spread of about 15 keV (1σ) consistent with that estimated from beam dynamics calculations [35]. After energy tuning, the proton beam is transported along the beam line and tuned onto LiLiT using two (electron-suppressed) Faraday cups, four wire profilers, a current reading from collimators, as well as the thermocouple temperature readings on the LiLiT duct side plates ("ears") [24,34] (Fig. 2). Tuning of the beam onto LiLiT starts at a 5% duty cycle using the SARAF slow chopper, ramping up slowly (20–30 min) to 99%. During the process, temperature and radiation are monitored along the beamline and on LiLiT while applying fine tuning on the beamline steerers. Following beam ramping-ups, when required, are performed faster (≈ 1–2 min). In order to determine the proton beam centering over an irradiation experiment, autoradiographic scans of gold foil monitors at the irradiation target position (see Fig. 3 and below) were made after the irradiation. A scan of one of the Au foils used in the (n, γ) run is presented in Fig. 4. A vertical offset (less

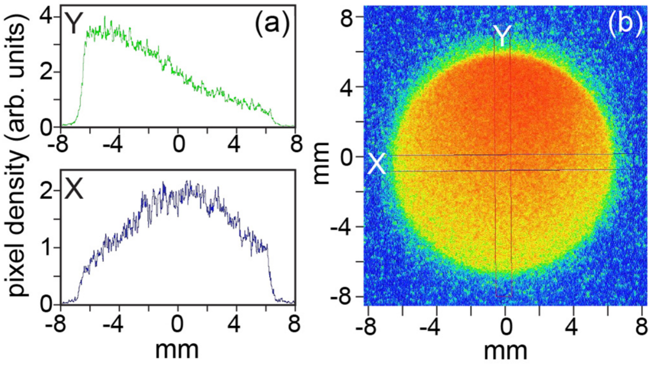

FIG. 4. (b) An auto-radiographic scan of the 13 mm diameter gold foil from the Kr irradiation above neutron production threshold. Colors indicate activity, decreasing from red to blue. (a) Profiles of a vertical (X) and horizontal (Y) slice of the scan. A vertical offset in neutron distribution (4.8(2) mm) is observed attributed to vertical steering of the proton beam. This offset is taken into account in the simulations.

controlled by the beam diagnostics at high intensity) of up to a few mm is usually found and in the present experiment was of 4.8(2) mm. This offset is accounted for in our neutron simulations (see below). Throughout the irradiation, the neutron yield was continuously monitored and recorded with a fission-product ionization chamber detector (PFC16A, Centronics Ltd.), counting neutron-induced fission events from a thin ^{235}U internal foil (1 mg/cm^2, 12.5 cm^2 active area). The fission chamber was located at 0° relative to the incident proton beam at a distance of ≈80 cm downstream the target. The fission chamber was covered with a 1 mm thick Cd sheet to absorb scattered thermal neutrons. The count rate of the fission chamber was calibrated to the beam current measured at low intensity with the current reading of the beam-line Faraday cup close to LiLiT. The time dependence of the neutron yield information is used for correction of the final activity measured for nuclides with half-lives short compared to irradiation time (see Section IV). The calibration of the fission chamber rate against the current reading at the Faraday cup was verified upon the end of irradiation.

A 10 mm outer diameter, 0.2 mm thick Ti spherical shell was filled with 107.7 mg (7.74×10^{20} atoms) of atmospheric Kr gas collected before the nuclear age [36]; contemporary atmospheric Kr is known to have elevated levels of fissiogenic ^{85}Kr (see *e.g.* [37]). The presence of cosmogenic ^{81}Kr in atmospheric Kr will be taken into account (see Section IV). After evacuation, Kr was deposited cryogenically at liquid nitrogen temperature in the Ti sphere. A photograph of the sphere gas container is presented in Fig. 3. The Ti sphere [33] filled with Kr, was positioned in the LiLiT target chamber centered at 11 mm downstream of the lithium free surface (Fig. 3). Two Au foils (≈12.5 μm thick) positioned in front of the Kr capsule, monitored the incident neutron fluence. A ZrO$_2$+Al pellet ≈ 1 mm thick was inserted as a parasitic target related to an independent experiment between the two Au foils. The pellet has negligible effect (≈1%) on the neutron fluence intercepted by the Kr gas and on the neutron energy spectrum (see below Fig. 6).

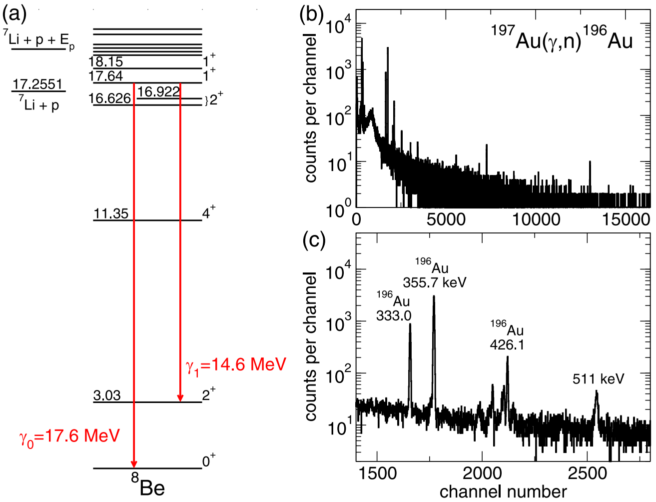

FIG. 5. (a) Part of the ^{8}Be energy level scheme. The two high energy γ's at 14.6 and 17.6 MeV are shown in red. See [23] for more details. (b) Spectrum of the ^{196}Au decay from the ^{197}Au$(\gamma, n)^{196}$Au reaction in a Au monitor foil for the under threshold run (irradiation *B*). (c) Zoom in on the relevant photopeaks in the spectrum.

The LiLiT setup above is known to produce, together with the ^{7}Li(p, n) neutrons, a copious amount of high-energy γ rays (mainly 17.6 and 14.6 MeV) from the ^{7}Li(p, γ) reaction [38] (Fig. 5). These γ rays, above neutron separation energy, can produce ^{A}Kr$(\gamma, n)^{A-1}$Kr reactions on stable ^{A}Kr isotopes and interfere with some of the (n, γ) measurements. In order to disentangle the two effects, two separate irradiations were performed in this work. The first one, described previously, at proton energy 1930 keV, just above the neutron production threshold and denoted by *A*, was performed with pre-nuclear-age Kr. A second irradiation, denoted by *B*, at proton energy (E_p = 1816 keV) below the neutron production threshold, where only the high-energy γ rays are emitted, was performed in order to correct for (γ, n) products. A contemporary atmospheric gas sample, contained in a separate Ti sphere, was used in irradiation *B* due to unavailability of pre-nuclear Kr, requiring an additional correction for fissiogenic ^{85}Kr presence in the sample. The (γ,n) corrections are small and discussed in Section IV. The contemporary Kr gas sample was required also to correct for the cosmogenic ^{81}Kr content of atmospheric Kr [36,39] in both irradiated samples; the cosmogenic abundance of ^{81}Kr, shielded from fission products by ^{81}Br, is the same within 1% in pre- and post-nuclear age Kr [39]. The gas samples used and irradiation details are presented in Table I.

TABLE I. Kr samples used in this work. Sample 43 was pre-nuclear Kr gas and samples 59 and 52 were post-nuclear Kr gas from same batch.

Sphere #	Irrad.	Reaction	Kr (mg)	E_p (keV)	Charge (mA h)
43	*A*	(n, γ)+(γ, n)	107.7	1930	7.28
59	*B*	(γ, n)	177.54	1816	11.7
52		not irrad.	490.99		

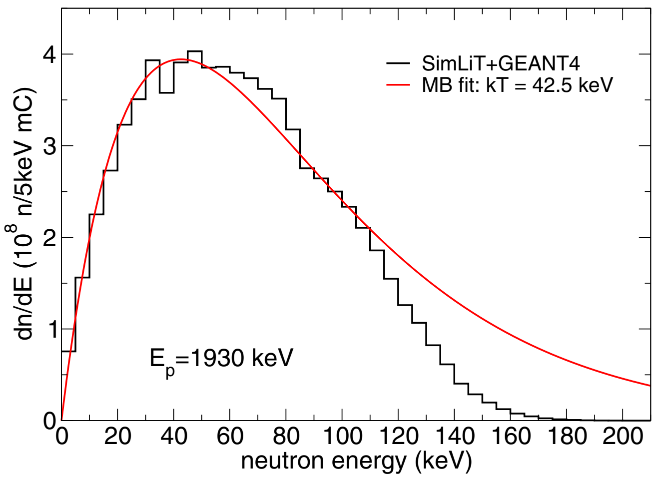

FIG. 6. Simulated neutron spectrum (black histogram) impinging on the Kr, $\frac{dn_{\rm sim}}{dE_n}$. Also shown is a fit to Maxwell-Boltzmann (MB) distribution (red curve) $E_n e^{-\frac{E_n}{kT}}$ at 42.5 keV in the range of 0–120 keV.

The experimental cross section measured in this work is an energy-averaged value over the neutron spectrum seen by the targets which, under the SARAF-LiLiT irradiation conditions, is not measurable. Instead, we rely on detailed Monte Carlo simulations using the codes SimLiT [40] for the thick-target ^{7}Li(p, n) neutron production and Geant4 [41] for neutron transport and scattering through the structural materials and targets (Fig. 6) [23,38]. The proton beam energy, energy spread, offset (see Fig. 4) as well as the geometrical position of the activation targets (Au foil, ZrO$_2$+Al pellet, Au foil, and Kr filled sphere), and all surrounding material were introduced into the simulations. The SimLiT-Geant4 simulations have been carefully benchmarked in separate experiments [23,38,40,42]. The simulated neutron spectrum, $\frac{dn_{\rm sim}}{dE_n}$ (Fig. 6), is well fitted in the range $E_n \approx 0$–120 keV ($\approx$93% of the incident neutrons) by a MB flux with $kT = 42.5$ keV. The simulated spectrum is later used for extrapolating the experimental energy-averaged cross section to one averaged over a true MB spectrum (see Sec. IV). The quantitative normalization of the neutron spectrum was obtained by comparing the experimental number of ^{198}Au nuclei in the Au foil monitors (measured by γ activity with a high-purity germanium detector, see Sec. III) with the number of ^{198}Au nuclei calculated in the simulation of the entire setup and scaled to the experimental proton charge (see [23] for details). For the gold activation simulation, we use ENDF/B-VIII.0 [43] which was checked carefully and found to be consistent with experimental data [44,45]. We note that the ^{198}Au measured and simulated activity normalized by the measured proton charge in this run agree within 1%. The under-threshold run was similarly monitored via the ^{196}Au activity from the ^{197}Au(γ, n) ^{196}Au reaction (see Fig. 5).

III. EXPERIMENTAL METHOD B: DETECTION OF REACTION PRODUCTS

After each of the SARAF-LiLiT irradiations A and B, the activities of the short-lived Kr isotopes (^{79,85m,87}Kr) were measured with a high-purity germanium (HPGe) detector (Ortec GMX25-83, Ser. No. 53-N13229A). The detector efficiency was determined by standard calibrated radioactive sources: ^{22}Na, ^{60}Co, ^{88}Y, ^{137}Cs, ^{152}Eu, and ^{155}Eu. Each sphere was positioned in front of the HPGe detector centered at 50 mm from its Be window with the stem immersed in a lead brick to reduce its γ background (Fig. 7). The decay properties of the relevant target and product nuclei used in this work are presented in Table II. For irradiation A, a series of 18 half-hour γ counting runs, starting $\approx$2.5 h after the end of the irradiation were measured; $\approx$1.5 days later another six 4 h runs were measured. A similar series was performed for irradiation B. Figures 8 and 9 illustrate γ spectra obtained in each case. The photopeaks from the decay of ^{79}Kr, ^{85m}Kr and ^{87}Kr are labeled in the spectra. Decay curves of ^{79,85m,87}Kr for irradiation A are presented in Fig. 10. The fitted half-lives obtained are 34.98(3), 4.483(3), and 1.264(9) h for ^{79,85m,87}Kr, respectively, in good agreement with the literature values presented in Table II. The time dependence of ^{85m}Kr decays via β^- extracted from the γ photopeak at 151.2 keV [75.2(5)% intensity], and via IT extracted from the γ photopeak at 304.9 keV [14.0(3)% intensity] is shown in Fig. 11. The ratio 0.188(9) of the yields of the 304.9 keV IT in ^{85m}Kr decay and the 151.2 keV β-delayed γ transition in ^{85}Rb agrees with the adopted value 0.186(4) [49] (see Table II). The number of activated nuclei produced in each irradiation is given in Sec. IV.

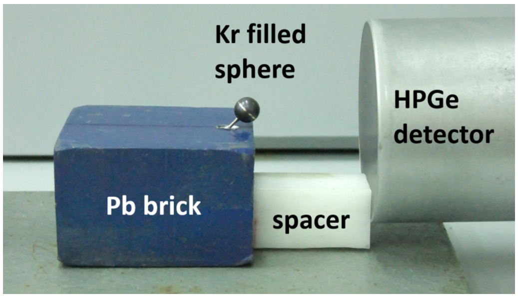

FIG. 7. Setup of the sphere placed in the lead brick with the stainless steel "stem" shielded by the lead and the Ti sphere, centered at 5 cm from the thin Be window on the face of the HPGe detector.

After measuring the short-lived isotopes, aliquots of the activated Kr samples were sent for atom trap trace analysis to the TRACER Center (ANL) and for low-level counting to University of Bern in order to measure the long-lived Kr isotopes (^{81,85g}Kr).

Atom trap trace analysis is a highly sensitive and selective atom-counting method for determining the isotopic abundance of rare noble gas radionuclides [51,52]. ATTA uses laser cooling and trapping techniques of neutral atoms to capture and detect the isotopes of interest. It exploits the frequency difference between isotopes (isotope shifts) as well as the narrow-band resonant nature of the atomic transitions used for laser manipulation and detection. Capture and detection of each atom requires many thousand successive atom-photon interactions of a closed-loop (cycling) atomic transition. Thus, by tuning the frequency of the laser light to match the transition in the isotope of interest, for example ^{81}Kr or ^{85}Kr

TABLE II. Properties of the relevant target and product nuclei used in this work.

Target nucleus	Natural abundance	Product nucleus	Half-life, $t_{\frac{1}{2}}$	Decay mode	γ-ray energy, E_γ (keV)	Intensity per decay, I_γ (%)	Ref.
^{197}Au	1	^{198}Au	2.6947(3) d	β^-, 100%	411.80205(17)	95.62(6)	[46]
^{78}Kr	$3.55(3)\times10^{-3}$	^{79m}Kr	50(3) s	IT, 100%			[47]
		^{79g}Kr	35.04(10) h	$\epsilon+\beta^+$, 100%	261.29(10)	12.7(4)	
					397.54(10)	9.3(4)	
					606.09(10)	8.1(3)	
^{80}Kr	0.02286(10)	^{81m}Kr	13.10(3) s	IT, 99.9975(4)%			[48]
				ϵ, 2.5×10^{-3}%			
		^{81g}Kr	$2.29(11)\times10^5$ yr	ϵ, 100%			
^{84}Kr	0.56987(15)	^{85m}Kr	4.480(8) h	β^-, 78.8(5)%	151.195(6)	75.2(5)	[49]
				IT, 21.2(5)%	304.87(2)	14.0(3)	
		^{85g}Kr	10.739(14) yr	β^-, 100%	513.997(5)	0.434(10)	[49]
^{86}Kr	0.17279(41)	^{87}Kr	76.3(5) min	β^-, 100%	402.587(10)	50(3)	[50]

in these experiments (see Fig. 12), laser interactions with any other species are exponentially suppressed to a point that ATTA is completely free from background due to any other isotope, isomer, isobar, or atomic or molecular species. In addition, once atoms are captured in the magneto-optical trap (MOT) at the heart of the instrument, the fast-cycling photon-atom interaction allows detection down to the single-atom level via laser-induced fluorescence. This single-atom sensitivity is crucial for the detection of the extremely rare krypton radioisotopes of interest here. The present measurement is, however, different from the typical application of the ATTA technique which only requires the relative isotopic abundances between samples and the atmospheric levels to be measured (e.g., for determination of mean residence times of old groundwater or ice samples, see [52]). However, recent developments of absolute calibration methods for both ^{81}Kr and ^{85}Kr, discussed below, allow for this application of the ATTA technique to obtain nuclear cross section data.

The third-generation ATTA instrument and the respective measurement techniques have been described in detail previously [52,53] and will be covered here only briefly. Figure 13 shows a schematic of the ≈ 2 m long atomic beamline and vacuum chamber that (in addition to a separate laser system) constitute the main components of an ATTA instrument. Within a ultra-high vacuum environment (traveling from the left to the right in the figure), the neutral krypton atoms start in the atom beam source and traverse a laser-induced collimation and Zeeman slowing section before entering the magneto-optical trap (MOT). There, laser-induced fluorescence emitted by the atoms is imaged onto a sensitive charged-coupled device (CCD) camera. Sample analysis procedures for the experiments in this work are as follows: at the outset of the measurement, approximately 10 μl (STP) of Kr gas from the sample of interest are injected into the upstream end of the vacuum system. There, a fraction of the atoms are excited by a radio-frequency-driven discharge source to a metastable electronic state, which is the lower level of the closed-loop

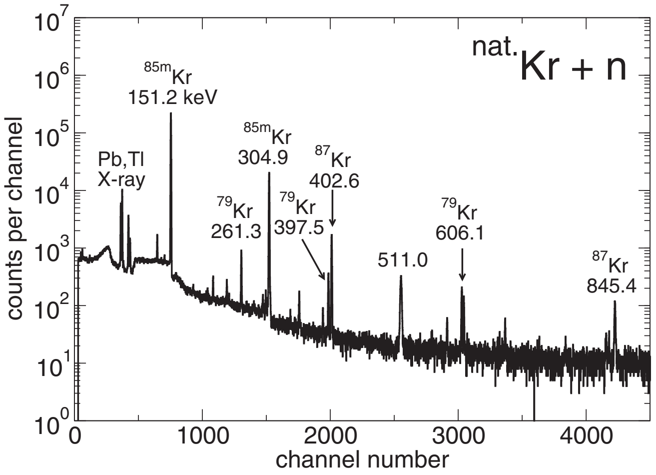

FIG. 8. γ-ray spectrum obtained by counting sphere #43 activity for 1872 s, starting 9007 s after end of irradiation *A* with an unshielded HPGe detector. The photopeaks from the decay of the activated Kr(n,γ) isotopes are labeled in keV.

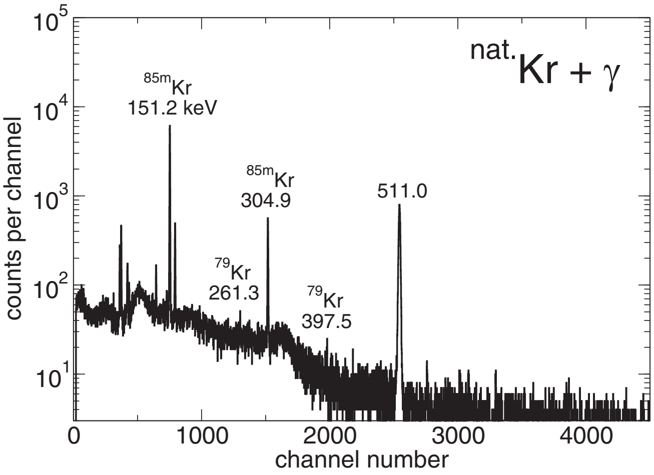

FIG. 9. γ-ray spectrum obtained by counting sphere #59 activity for 7208 s, starting 2844 s after end of irradiation *B* with a shielded HPGe detector. The photopeaks from the decay of the activated Kr(γ,n) isotopes are labeled in keV.

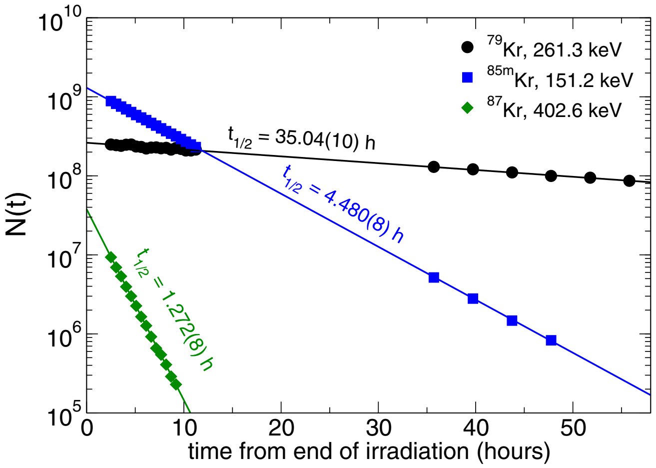

FIG. 10. Decay curves of ^{79,85m,87}Kr. The half-lives obtained from exponential fits of the curves (see text) are in good agreement with the adopted values in the literature (labeled in the figure).

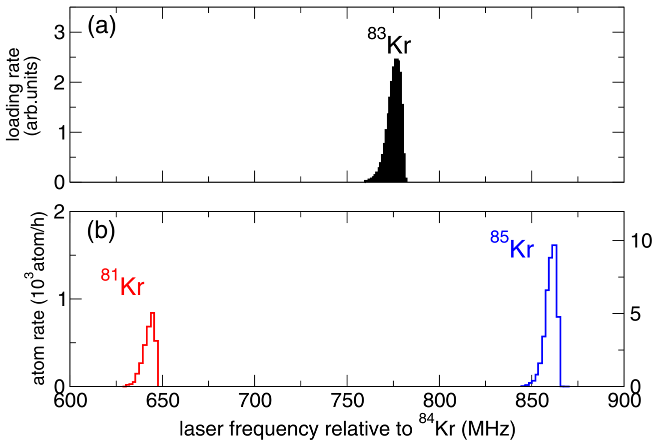

FIG. 12. Typical spectrum of the trap capture rate of ^{81,83,85}Kr versus laser frequency shift (relative to a reference transition in stable ^{84}Kr) measured for an atmospheric Kr sample (^{81}Kr/Kr = 9.3×10^{-13} [39]). Figure adapted from [52], see text.

atomic transition used for laser manipulation in the following stages. As such, only atoms in this metastable state are then laser cooled and captured into the MOT and detected by the CCD camera. Figure 13 displays the CCD signals versus time for a selected region of interest over the course of the measurement.

Since the resonant nature of the laser excitation processes ensures that only the isotope of interest is loaded into the trap, during the course of a measurement, the laser frequency is cycled with a 5-minute sequence to alternatingly load rare (^{81}Kr or ^{85}Kr) and stable (^{83}Kr) isotopes (where the laser frequency for trapping a given isotope is set to the frequency at the peak loading rate of the isotope shown in Fig. 12). Isotopic ratios are then determined by comparing the loading rates of the rare and stable isotopes over the course of the measurement, which lasts a total of 2–3 hours. During this time span the sample gas is continuously recirculated in the vacuum system back to the atom source. This recirculation reduces the sample size required for one measurement by more than four orders of magnitude.

The rare isotope capture rate is determined by counting the individual atoms over time and the experimental uncertainty is typically dominated by the statistical counting error. In order to obtain the atom count, atoms are loaded into the trap for 290 ms, the CCD camera is then exposed for 50 ms to detect the laser-induced fluorescence, and subsequently the trap is emptied via a 10 ms quench laser light pulse. This cycle is repeated for a few minutes before switching to the stable or

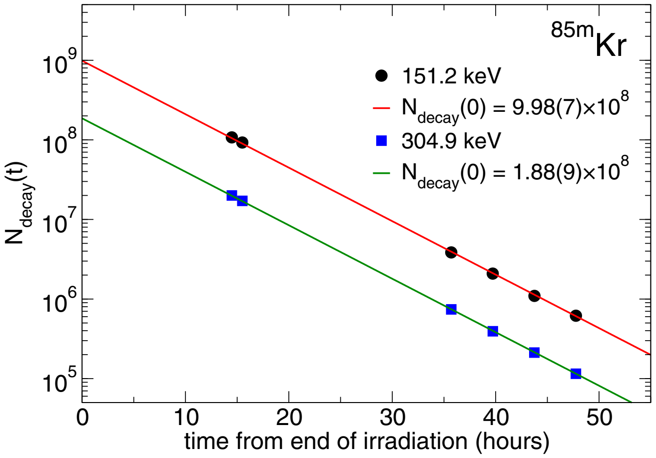

FIG. 11. The number of ^{85m}Kr decaying via β^- calculated from the γ photopeak at 151.2 keV [75.2(5)% intensity], and via IT calculated from the γ photopeak at 304.9 keV [14.0(3)% intensity]. The measured ratio is 0.188(9) in good agreement with the intensity ratio 0.186(4) in [49] (see Table II).

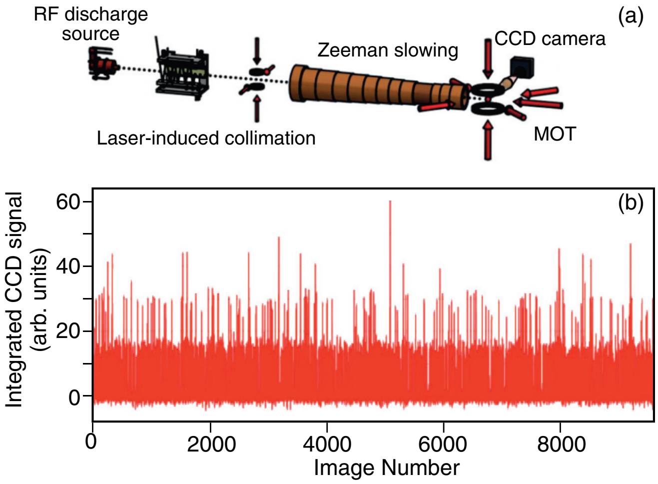

FIG. 13. (a) Schematic of the ATTA atomic beamline. Atoms (dotted line) travel from left to right, starting at the radio-frequency discharge source, passing through laser-induced collimation and Zeeman slowing stages, and ending in the MOT where they are imaged by a CCD camera. (b) Integrated CCD camera signal (divided by 1000) over a region of interest during the ^{81}Kr trapping cycles over the course of measuring the Kr gas sample (irradiation *B*) displayed vs time. Zero-, one- and two-^{81}Kr atom trapping events are observed.

other rare isotope. A single point on the time stream of CCD data shown in Fig. 13 represents the integrated signal from a region of interest on the CCD camera for the case of ^{81}Kr. At the end of the measurement, the time stream data from Fig. 13 are converted to a histogram enabling the counting of 0, 1, 2, or more individual atoms in the trap based on the discrete signal levels. The stable isotope loading rate, because it is so much larger, is measured by monitoring the dominant trap loss rate in the steady state when the atoms are continuously loaded into the trap. This dominant loss is due to Penning ionization, which leads to the formation of krypton ions in the trap. An electric field created by high-voltage electrodes in the MOT vacuum chamber directs these ions onto a Faraday cup near the trap. The respective ion current is at the nA level and proportional to the trap loading rate of the stable isotope. This ion method for measuring the stable loading rate is described in detail in [53] and the experimental uncertainty is determined from the variance of the measured ion current.

In order to determine the sample's ^{81}Kr and ^{85}Kr isotopic abundances, a measurement of a reference gas with known ^{81}Kr and ^{85}Kr isotopic abundances is conducted immediately after the sample measurement. The resulting super-ratio of the isotopic ratio measurements in the sample and those in the reference gas thus provides the ^{81}Kr and ^{85}Kr isotopic abundances of the sample relative to that of the reference gas. It should be noted that by conducting this reference measurement on the same day as the sample measurement we eliminate systematic effects on isotope ratios related to slow drifts in laser alignment and conditions in the atom source, which can vary at the percent level over the course of several days. The only difference then between the sample and reference measurements is that the reference gas is measured with gas constantly flowing through the system (i.e., not recirculated) in order to avoid cross-contamination of the reference gas with the irradiated sample (see [54,55] for details). In order to account for any systematic difference between these two modes of gas flow during an analysis, additional measurements are conducted where the reference gas is treated as if it were a sample. Deviations of the super-ratio from unity in these measurements indicate systematic effects, which are included as corrections in the measurements of the irradiated samples in this work.

Because ATTA, as described above, is a relative measurement method, the determination of the absolute isotopic abundances in the reference gas is crucial in order to achieve the isotopic abundance determination of the irradiated samples. This is done in different ways for the two isotopes of interest. For ^{85}Kr, the isotopic abundance of the reference gas was determined by LLC at University of Bern to be 32.1(12) dpm/cm^3 [equivalent to $^{85}\mathrm{Kr}/\mathrm{Kr} = 9.7(4) \times 10^{-12}$] as of March 3, 2016. The reference gas was recently validated by an inter-laboratory comparison [56]. Additionally, the University of Bern has also provided TRACER a series of samples spanning over an order of magnitude in ^{85}Kr isotopic abundances, to validate the linearity of the measurement technique [52,55]. For ^{81}Kr, the reference gas is the ^{81}Kr isotopic abundance in modern atmospheric Kr. This value was recently redetermined [39] by ATTA measurements on a dilution series of an enriched ^{81}Kr sample analyzed for ^{81}Kr abundance by noble-gas mass spectrometry; see details in [39]. The measurement yielded a value $^{81}\mathrm{Kr}/\mathrm{Kr} = 9.3(3) \times 10^{-13}$ in modern atmosphere, higher than that measured in 1969 [$^{81}\mathrm{Kr}/\mathrm{Kr} = 6.6(7) \times 10^{-13}$] by Loosli and Oeschger [36]. The newly determined value was used in this work.

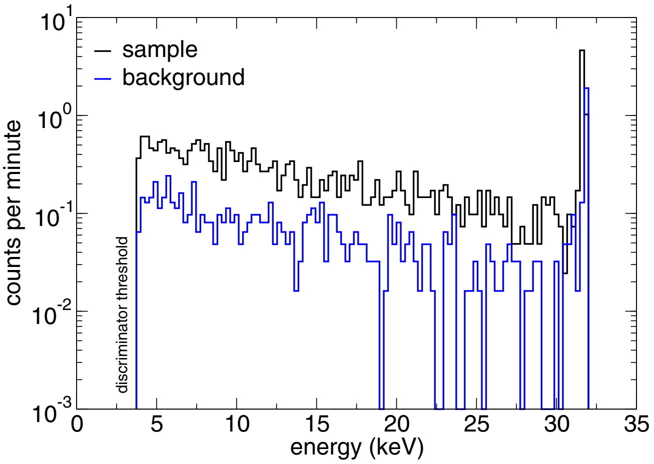

FIG. 14. Sample (upper histogram) and background (lower) β spectra for measurement 1. Only a fraction of the particle decay energy (687 keV) is released within the counter before they reach its wall. Events with energies greater than 33 keV are recorded as saturated events in the last MCA channels and are included in the ^{85}Kr activity analysis.

For irradiation *A* (above neutron threshold), the ^{85g}Kr was also measured at University of Bern by low-level proportional β counting. The Kr gas is transferred into a copper counter by means of a P10 carrier and filling gas (10% CH$_4$, 90% Ar). The counter with volume of 22 cm^3 is operated in the underground laboratory of the University of Bern [57] at a filling pressure of 2360 mbar. The spectrum (Fig. 14) is recorded by a 7-bit multichannel analyzer (MCA) with a linear energy range of 0–35 keV [58]. A background spectrum with Kr-free P10 gas is subtracted for calculating the net count rate. The counting efficiency in the energy range 4–35 keV is 48.4(4)% (see [56]). The amount of Kr in the counter was determined after the activity measurement by mass spectrometry (Table III). The mean net activities of two independent measurements (Table III) resulted in an activity concentration of 5.9(4) dpm/cm^3 Kr (STP) which corresponds to $^{85}\mathrm{Kr}/^{84}\mathrm{Kr} = 3.2(2) \times 10^{-12}$.

Finally the 514 keV photopeak from the decay of ^{85g}Kr ($t_{1/2} = 10.7$ yr) was also measured (with limited statistics) at the Goethe University in Frankfurt for ≈ 16 days with a HPGe

TABLE III. Counting parameters of two ^{85}Kr measurements. dpm/cm^3 refers to cm^3 of Kr STP. 1 dpm/cm^3 corresponds to an isotopic abundance of $^{85}\mathrm{Kr}/\mathrm{Kr} = 3.03 \times 10^{-13}$.

Meas.	Counting time (min)	Kr (μl)	Activity (dpm)	Specific act. (dpm/cm^3)
1	8000	37.1(8)	0.22(2)	5.9(6)
2	3600	99.3(10)	0.59(5)	5.9(5)

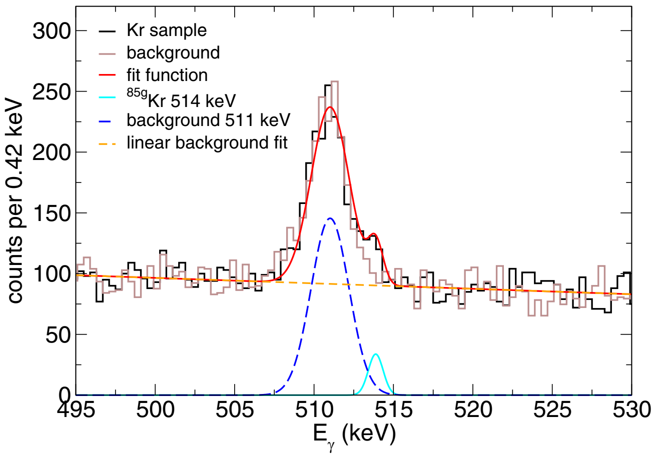

FIG. 15. 514 keV photopeak next to the 511 keV photopeak for the irradiation above neutron production threshold. This region in the spectrum was fitted to two Gaussians and a linear background. The amount of ^{85g}Kr produced during the irradiation was determined from this fit (see Table V).

detector. The spectrum obtained is presented in Fig. 15. The experimental results and comparison of measurements performed via different techniques are presented in next Sec. IV.

IV. EXPERIMENTAL RESULTS

The number of activated nuclei created during the irradiation, $N_{\rm act}$, for ^{79,85m,87}Kr was obtained from the γ spectra using

$$N_{\rm act} = \frac{C}{\epsilon_\gamma I_\gamma K_\gamma} \frac{e^{\lambda t_{\rm cool}}}{1 - e^{-\lambda t_{\rm real}}} \frac{t_{\rm real}}{t_{\rm live}} \frac{1}{f_b}, \tag{2}$$

where C is the number of counts in the photopeak, ϵ_γ is the detector photoelectric efficiency, I_γ is the γ intensity per decay, K_γ is the correction due to γ-ray self-absorption in the sample and in the Ti sphere shell (calculated here with a GEANT4 [41] simulation). $\lambda = \frac{\ln(2)}{t_{1/2}}$ is the decay constant of the activated nucleus, $t_{\rm cool}$ is the time between the end of the irradiation and the activity measurement, $t_{\rm real}$ is the real measuring time, and $t_{\rm live}$ is the live measuring time. f_b accounts for the decay of activated nuclei during the activation; f_b is calculated using the time dependence of the neutron yield $\Phi(t)$ obtained from the fission chamber by $f_b = \frac{\int_0^{t_a} \Phi(t) e^{-\lambda(t_a - t)} dt}{\int_0^{t_a} \Phi(t) dt}$. The decay parameters and correction factors used in the analysis are listed in Tables II and IV. For the decay counting measurements (γ counting and LLC), the isotopic abundances $^{A+1}$Kr / ^{A}Kr, used for the extraction of the experimental cross sections (see below), are calculated from the $N_{\rm act}$ values and the number of ^{A}Kr target atoms (see Table I). The atom counting measurements (ATTA) directly yield the $^{A+1}$Kr / ^{A}Kr isotopic abundance in the gas sample.

TABLE IV. Data analysis example of the HPGe data from the Kr sphere above threshold, measured 16 480 s after end of irradiation *A*, for a real time of 1852.5 s and a live time of 1800 s.

Nuclei	E_γ (keV)	Counts	ϵ_γ (10^{-2})	K_γ	f_b
^{79}Kr	261.3	4044(74)	1.31(3)	0.99(1)	0.915
	397.5	1994(50)	0.912(23)	0.99(1)	0.915
	606.1	1167(38)	0.648(16)	0.99(1)	0.915
^{85m}Kr	151.2	712 587(850)	2.01(5)	0.98(1)	0.542
	304.9	71 035(283)	1.07(3)	0.99(1)	0.542
^{87}Kr	402.6	3194(61)	0.905(23)	0.99(1)	0.233

TABLE V. Summary of the number of activated nuclei $N_{\rm act}$ and isotopic abundances $^{A+1}$Kr / ^{A}Kr produced at the end of irradiation *A* (above neutron threshold; see Table I for Kr sample mass and irradiation charge). For ATTA measurements, the value directly measured is quoted.

$^{A+1}$Au, $^{A+1}$Kr	ATTA value	$\frac{^{A+1}\text{Kr}}{^{A}\text{Kr}}$ (10^{-12})	$N_{\rm act}$ (10^8)	Det. meth.
^{198}Au			255(6)	γ spect.
^{79}Kr		101(4)	2.76(11)	γ spect.
^{81}Kr	2.370(56)[a]	96.2(39)[b]	17.1(7)	ATTA
^{85m}Kr		5.62(18)	24.6(8)	γ spect.
^{85g}Kr[c]	6.12(21)[d]	3.26(11)[b]	14.4(5)	ATTA
^{85g}Kr[c]		3.16(18)	13.9(9)	LLC
^{85g}Kr[c]		2.63(88)	12(4)	γ spect.
^{87}Kr		1.16(8)	1.55(10)	γ spect.

[a] $(^{81}\text{Kr}/\text{Kr})_{\rm sample}/(^{81}\text{Kr}/\text{Kr})_{\rm atm}$; $(^{81}\text{Kr}/\text{Kr})_{\rm atm}$ was determined in an absolute way by ATTA [39].

[b] The ratio measured by ATTA was converted to $^{A+1}$Kr / ^{A}Kr ratios using the Kr natural abundances.

[c] Yield of ^{85g}Kr (prompt+IT); see Table II.

[d] dpm/cm^3 cross-calibrated by LLC.

TABLE VI. Summary of the number of activated nuclei $N_{\rm act}$ from (γ, n) reactions and from preexisting nuclei in the contemporary Kr used and corresponding isotopic abundances at the end of irradiation *B* (below neutron threshold; see Table I for Kr sample mass and irradiation charge). The activated isotope $^{A+1}$Kr listed in column 1 is produced by the $^{A+2}$Kr$(\gamma, n)^{A+1}$Kr reaction. However, note that the isotopic abundances are listed identically as in Table V.

Au, $^{A+1}$Kr	ATTA value	$\frac{^{A+1}\text{Kr}}{^{A}\text{Kr}}$ (10^{-12})	$N_{\rm act}$ (10^8)	Det. method
^{196}Au			0.50(2)	γ spect.
^{79}Kr		0.245(17)	0.0111(8)	γ spect.
^{81}Kr	0.96(3)[a]	38.9(18)[b]	11.4(5)	ATTA
^{85m}Kr		0.0123(4)	0.090(2)	γ spect.
^{85g}Kr[c]		5.4(11)	39(8)	γ spect.
^{85g}Kr[c]	8.28(34)[d]	4.39(18)[b]	32(1)	ATTA

[a] $(^{81}\text{Kr}/\text{Kr})_{\rm sample}/(^{81}\text{Kr}/\text{Kr})_{\rm atm}$; $(^{81}\text{Kr}/\text{Kr})_{\rm atm}$ was determined in an absolute way by ATTA [39].

[b] The ratio measured by ATTA was converted to $^{A+1}$Kr / ^{A}Kr ratios using the Kr natural abundances.

[c] Yield of ^{85g}Kr (prompt+IT); see Table II.

[d] dpm/cm^3 cross-calibrated by LLC.

TABLE VII. Summary of the number of ^{81,85}Kr nuclei in the nonirradiated contemporary Kr. The isotopic abundances, $^{A+1}\mathrm{Kr}/^{A}\mathrm{Kr}$, are listed identically as in Table V. The contemporary Kr sample was taken from the same gas cylinder as that used in irradiation *B*.

$^{A+1}$Kr	ATTA value	$\frac{^{A+1}\mathrm{Kr}}{^{A}\mathrm{Kr}}$ (10^{-12})	N_{act} (10^{9})	Det. method
^{81}Kr	0.99(3)[a]	40.2(18)[b]	3.2(1)	ATTA
^{85g}Kr		4.74(35)	9.6(8)	γ spect.
^{85g}Kr	8.03(28)[c]	4.26(16)[b]	8.6(3)	ATTA

[a] $(^{81}\mathrm{Kr}/\mathrm{Kr})_{\mathrm{sample}}/(^{81}\mathrm{Kr}/\mathrm{Kr})_{\mathrm{atm}}$; $(^{81}\mathrm{Kr}/\mathrm{Kr})_{\mathrm{atm}}$ was determined in an absolute way by ATTA [39].

[b] The ratio measured by ATTA was converted to $^{A+1}\mathrm{Kr}/^{A}\mathrm{Kr}$ ratios using the Kr natural abundances.

[c] dpm/cm^3 cross-calibrated by LLC.

Tables V and VI list the isotopic abundances and number of activated nuclei determined respectively for irradiations *A* and *B* (see Table I). The isotopic abundances measured for *A* by ATTA and LLC are in agreement, confirming the ATTA normalization via LLC for ^{85}Kr determination. We note that the value measured independently by γ spectrometry is also consistent. The ^{81,85g}Kr isotopic abundances measured for the nonirradiated contemporary Kr gas used in *B* are given in Table VII. The latter values, originating from (mainly) cosmogenic ^{81}Kr and fissiogenic ^{85}Kr are used to correct abundances measured for irradiation *B*. The final net values of isotopic abundances $^{A+1}\mathrm{Kr}/^{A}\mathrm{Kr}$ produced by (n,γ) reactions only in irradiation *A* are obtained by subtracting (γ,n) yields from the yields measured in irradiation *A* and are listed in Table VIII. A correction was applied for the dependence of the γ yield of the $^{7}\mathrm{Li}(p,\gamma)$ reaction in the proton incident energy above (irradiation *A*) and below (irradiation *B*) neutron threshold. The γ yield dependence was taken from [59] by extrapolation to the appropriate proton energies. See the Appendix for extraction of experimental (γ,n) cross sections from our data.

TABLE VIII. Summary of the net number of nuclei activated via the $^{A}\mathrm{Kr}(n,\gamma)$ reactions (N_{act}) and the corresponding $\frac{^{A+1}\mathrm{Kr}}{^{A}\mathrm{Kr}}$ ratio. Results from the above-threshold irradiation *A* (Table V) were corrected for (γ,n) reactions by an under-neutron-threshold irradiation *B* (Table VI) and for cosmogenic and fissiogenic abundances of ^{81,85g}Kr of contemporary Kr (Table VII).

$^{A+1}$Au, $^{A+1}$Kr	$\frac{^{A+1}\mathrm{Kr}}{^{A}\mathrm{Kr}}$ (10^{-12})	N_{act} (10^{9})	Det. method
^{198}Au		25.5(6)	γ spect.
^{79}Kr	101(4)	0.276(11)	γ spect.
^{81}Kr	57(3)	1.01(5)	ATTA
^{85m}Kr	5.62(18)	2.46(8)	γ spect.
^{85g}Kr[a]	3.2(2)	1.40(8)	ATTA
^{87}Kr	1.16(8)	0.155(10)	γ spect.

[a] Yield of ^{85g}Kr (prompt+IT); see Table II.

TABLE IX. Summary of experimental averaged cross sections σ_{exp} and correction factors $C_{\mathrm{JEFF}}(30\ \mathrm{keV})$ in this work.

Isotope	$\frac{2}{\sqrt{\pi}}\sigma_{\mathrm{exp}}$ (mb)[a]	$C_{\mathrm{JEFF}}(30\ \mathrm{keV})$
^{78}Kr	407 ± 20	0.967(7)
^{80}Kr	230 ± 14	1.11(2)
^{84}Kr[b]	30.7 ± 2.4	1.13(3)
$^{84}\mathrm{Kr}\rightarrow{}^{85m}$Kr[c]	22.6 ± 1.0	1.13(3)
$^{84}\mathrm{Kr}\rightarrow{}^{85g}$Kr (prompt+IT)[d]	12.9 ± 0.8	1.13(3)
$^{84}\mathrm{Kr}\rightarrow{}^{85g}$Kr (prompt)[e]	8.1 ± 0.8	1.13(3)
^{86}Kr	4.7 ± 0.3	1.08(2)

[a] The factor $2/\sqrt{\pi}$ (see [5]) enables a comparison with the MACS value (Table X).

[b] Prompt yield feeding ground and isomeric state, calculated from $\sigma_{\mathrm{exp}}(^{85m}\mathrm{Kr}) + \sigma_{\mathrm{exp}}(^{85g}\mathrm{Kr}\ \mathrm{prompt})$.

[c] ^{85m}Kr decays both by IT and by β^- decay; see Table II.

[d] Directly extracted from the ATTA measurement.

[e] Extracted by subtracting from the (prompt+IT) yield the contribution of the IT transition ($= 0.212 \times {}^{85m}$Kr yield; see Tables II and VIII).

The average experimental $^{A}\mathrm{Kr}(n,\gamma)$ cross sections, σ_{exp}, can be obtained from

$$\sigma_{\mathrm{exp}} = \frac{r}{\Phi_n}, \tag{3}$$

where $r = {}^{A+1}\mathrm{Kr}/^{A}\mathrm{Kr}$ is the isotopic ratio produced by $^{A}\mathrm{Kr}(n,\gamma)$ reactions at the end of irradiation (Table VIII) and Φ_n is the effective neutron fluence (n/cm^2) on the Kr sample. In the complex geometry of the spherical gas target, the neutron fluence is calculated using the SIMLIT-GEANT4 [40,41] simulation by the expression $\Phi_n = \frac{\sum l_n}{V}$, where l_n is the length traveled by a neutron in the gas and V is the volume of the gas sphere (0.46 cm^3). The sum $\sum l_n$ runs over a statistically representative sample of neutrons (1×10^7 neutrons generated). The value is then scaled by the ratio of measured to simulated activity of the Au monitor, calculated in the same simulation (see [23,60] for details and benchmarking of the method of fluence determination). Uncertainty in the value V leads to negligible correction in the value of the ratio $\Phi_n = \frac{\sum l_n}{V}$. The value of Φ_n for irradiation *A* is $2.78(6) \times 10^{14}\ n/\mathrm{cm}^2$; the uncertainty is determined by the simulations and their normalization to the Au monitor activity (see [23,38]). The results of the experimental cross sections, σ_{exp}, are presented in Table IX.

The Maxwellian averaged cross section (MACS) at a given thermal energy kT is calculated with the procedure developed in [23,38,60], using

$$\mathrm{MACS}_{\mathrm{exp}}(kT) = \frac{2}{\sqrt{\pi}} C_{\mathrm{lib}}(kT)\sigma_{\mathrm{exp}}, \tag{4}$$

where the correction factor $C_{\mathrm{lib}}(kT)$ is given by

$$C_{\mathrm{lib}}(kT) = \frac{\dfrac{\int_0^\infty \sigma_{\mathrm{lib}}(E_n) E_n e^{-\frac{E_n}{kT}}\, dE_n}{\int_0^\infty E_n e^{-\frac{E_n}{kT}}\, dE_n}}{\dfrac{\int_0^\infty \sigma_{\mathrm{lib}}(E_n)\frac{dn}{dE_n} dE_n}{\int_0^\infty \frac{dn}{dE_n} dE_n}}. \tag{5}$$

TABLE X. Comparison of the $\mathrm{MACS_{exp}}$(30 keV) measured in this work (using the JEFF-3.3 library [61]) with previously measured MACS. The units are mb.

Target / Ref.	^{78}Kr	^{80}Kr[a]	^{84}K[a]	$^{84\rightarrow85m}$Kr	$^{84\rightarrow85g}$Kr (prompt+IT)[b]	$^{84\rightarrow85g}$Kr (prompt)[c]	^{86}Kr
Raman [14]							4.8(12)
Walter [15][d]	332(40)	267(15)	37.7(46)				5.3(7)
Walter [16][d]							3.7(7)
Käppeler [17]				17.3(12)			3.6(3)
Beer [18]	318(26)			18.3(8)			3.34(24)
Tomyo [19]			32.5(27)				
Mutti [20]		290(2)[e]	33(2)				4.76(28)
This work	394(20)	257(16)	34.7(28)[f]	25.6(13)	14.6(10)	9.15(95)	5.07(37)

[a] Prompt yields feeding ground state and isomeric state as measured in time-of-flight experiments [15,19,20].
[b] Overall yield feeding ^{85g}Kr(10.8 y) via prompt + ^{85m}Kr(4.5 h) IT decay, directly measured in this work by ATTA.
[c] Extracted from the ^{85g}Kr (prompt+IT) yield $-$ 0.212 $\times$ ^{85m}Kr yield.
[d] Renormalized from original Ref. [62].
[e] Statistical uncertainty only.
[f] Calculated from $\sigma_{\mathrm{exp}}(^{85m}\mathrm{Kr}) + \sigma_{\mathrm{exp}}(^{85g}\mathrm{Kr\ prompt})$ (see Table IX).

In Eq. (5), $\frac{dn}{dE_n}$ is the simulated neutron spectrum $\frac{dn_{\mathrm{sim}}}{dE_n}$ (see Fig. 6), and $\sigma_{\mathrm{lib}}(E_n)$ is the energy-dependent neutron capture cross section taken from an evaluation library. The library *lib* used in this work is JEFF-3.3 [61]; the values obtained for $\mathrm{C_{JEFF}}$ are listed in Table IX. The uncertainty of the correction factor $C_{\mathrm{JEFF}}(kT)$ was taken as 20% of the correction $(|1 - C_{\mathrm{JEFF}}(kT)| \times 0.2)$. The uncertainties for ^{78}Kr and ^{80}Kr MACS at 30 keV are presented in Table XI. A comparison of the $\mathrm{MACS_{exp}}$ at 30 keV from this work to previously measured MACS [14–20] is shown in Table X and Fig. 16. Significant differences are observed for the activation cross section of the short-lived isotopes ^{79}Kr and ^{85m}Kr. Interestingly, the present data measured by activation and atom counting (ATTA) for the long-lived products ^{81}Kr and ^{85g}Kr are in fair agreement with previous time-of-flight (TOF) data. In particular, good agreement exists with the most recent TOF data of Mutti *et al.* [20] for all three Kr isotopes ^{81,85g,87}Kr measured in both data sets. The $\mathrm{MACS_{exp}}$ extrapolated to various kTs are presented in Table XII. The astrophysical reaction rates calculated with the MACS values of Table XII are illustrated in Fig. 17.

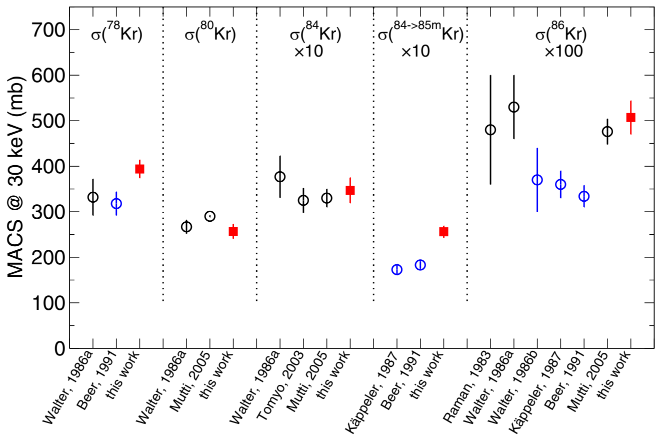

FIG. 16. Comparison of the $\mathrm{MACS_{exp}}$(30 keV) measured in this work (red squares) with previously measured MACS. Black (blue) open dots correspond to time-of-flight (activation) experiments.

V. ASTROPHYSICAL IMPLICATIONS

We calculated stellar models with different masses, a low-mass $2M_\odot$ model [63] and a massive $25M_\odot$ model [64] both with $Z = Z_\odot$, to assess the impact of our $^A\mathrm{Kr}(n,\gamma)$ cross section values on stellar nucleosynthesis simulations in the Kr-Rb-Sr-Y-Zr region of the nuclide chart. The models have been chosen considering that the asymptotic giant branch (AGB) phase of low-mass stars $(1 < M/M_\odot < 5)$ hosts the main component of the *s* process [65], while the weak component of the *s* process takes place during the core He burning and C-shell burning of massive stars (M > 10$\mathrm{M}_\odot$; see, e.g., [4]).

The stellar codes used to evaluate the effects induced by the new cross sections are the FUNS code [66] for the low-mass star model and the FRANEC code [67] for the massive star model. The evolution of the star is followed from the pre-

TABLE XI. List of uncertainties (in %) of $\mathrm{MACS_{exp}}$ at 30 keV in representative cases (^{78}Kr and ^{80}Kr). For ^{78}Kr all uncertainties are systematic besides the statistical.

Source of uncertainty	^{78}Kr	^{80}Kr
Kr mass	0.1	0.1
abundance	0.8	0.4
statistical (random)	0.3	
ATTA measurement		4.3
efficiency	2.5	
intensity	3.1	
self-absorption	1	
under-threshold correction	<0.1	
cosmogenic correction		3.2
simulation (for neutron fluence)	2	2
$\mathrm{C_{JEFF}}$	0.7	2.0
Total	4.7	6.1

TABLE XII. MACS obtained at various kT (using the JEFF-3.3 library [61]). The units are mb.

kT (keV)	^{78}Kr	^{80}Kr	^{84}Kr	$^{84\to85m}$Kr	^{86}Kr
3	962(121)	904(144)	278(54)	205(38)	2.83(43)
5	730(74)	699(102)	179(33)	132(23)	3.59(34)
8	629(54)	550(71)	115(19)	85(1)	4.63(33)
10	589(47)	487(58)	93(14)	68.4(97)	5.11(38)
20	464(26)	325(27)	48(5)	35.7(31)	5.62(44)
30	394(20)	257(16)	34.7(28)	25.6(13)	5.07(37)
40	351(21)	219(13)	28.5(22)	21.0(10)	4.45(32)
60	299(26)	179(15)	23.3(23)	17.1(13)	3.52(35)
80	268(31)	158(17)	21.5(25)	15.8(15)	2.92(41)
100	247(34)	145(19)	20.8(25)	15.3(16)	2.52(47)
150	211(41)	127(22)	20.5(26)	15.1(16)	1.95(57)
200	187(45)	116(24)	20.5(26)	15.1(17)	1.70(60)
300	154(51)	100(27)	20.0(26)	14.7(17)	1.58(63)

main-sequence phase and, passing through all nuclear burning stages, is evolved up to the complete erosion of the stellar envelope via strong stellar winds (in the case of low masses) or up to core collapse (in the case of massive stars). The feature that makes these codes unique is the coupling of a full nuclear network with the physical evolution of the structure. As a matter of fact, the production/destruction of each isotope is followed in detail for each shell layer from the stellar center to the surface, including the material ejected into the interstellar medium (which constitutes the stellar yields). In such a way, the complete feedback induced by nuclear burning is taken into consideration. Moreover, any approximation or loss of information related to the adoption of post-process techniques is avoided.

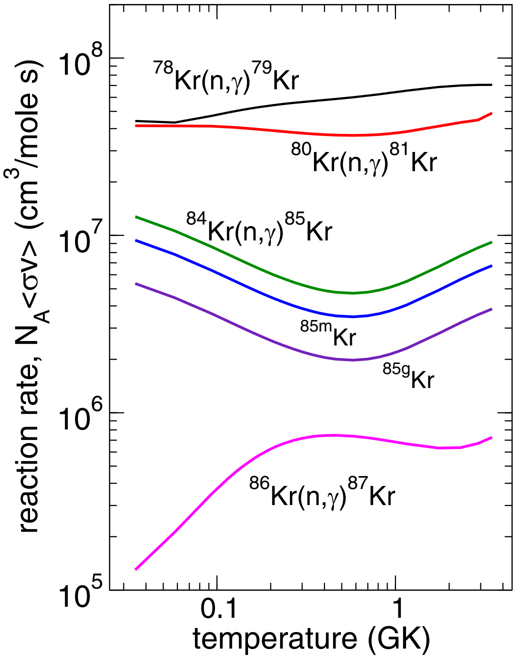

FIG. 17. Astrophysical reaction rates for (n, γ) reactions on Kr isotopes calculated with the MACS values of Table XII.

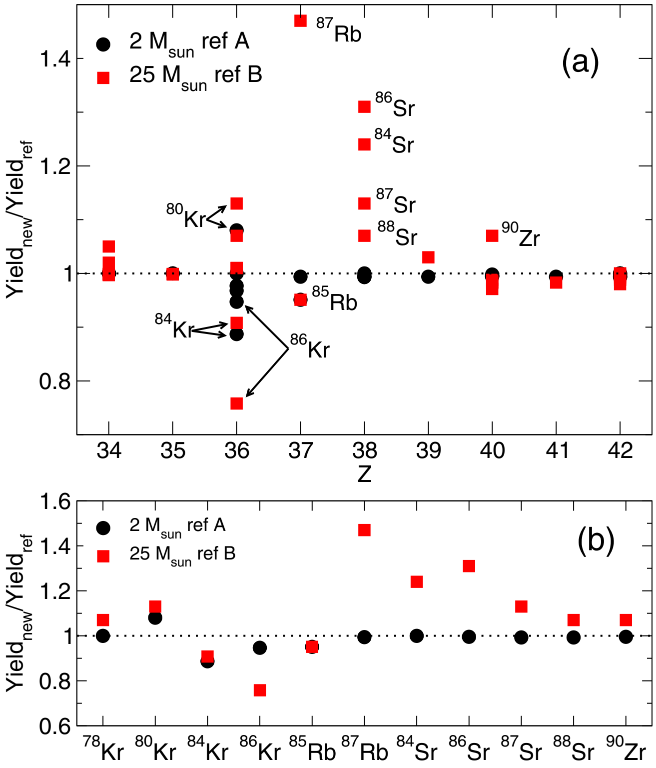

FIG. 18. Ratios between the yields obtained with cross sections measured in this work and those calculated with reference cross sections ref A (low-mass star) and ref B (massive star): (a) nuclides are grouped by atomic number; (b) selected nuclides whose yields differ by more than 5%. See text for details.

In Fig. 18 we plot the ratios between the stellar yields computed with the cross sections of this work and reference ones denoted by ref A for the low-mass star model and ref B for the massive star one. The two reference cross section sets are based on [15,16,18] but ref A was updated to more recent Kr data [20]. One of the most important results we obtain is the increase in the production of ^{80}Kr (+8% and +13%, in low and massive star models, respectively). ^{80}Kr belongs to a particular class of isotopes, named s-only, which entirely owe their cosmic production to the s process (see, e.g., [68]). The experimental study of these isotopes is therefore an extremely powerful tool to constrain s-process nucleosynthesis calculations, and in particular the physics of stars where it is at work. Recently, Prantzos *et al.* [6] highlighted a deficit ($\approx -15\%$) of ^{80}Kr in their galactic chemical evolution (GCE) model. The solar ^{80}Kr content is mainly provided by massive stars, whose contribution (≈80%) largely overwhelms that of low-mass stars. In massive stars, this isotope is produced during the O-shell burning by the photodisintegration sequence ^{87}Rb(γ, n) ^{86}Rb(γ, n) ^{85}Rb followed by ^{85}Rb(γ, p) ^{84}Kr that, in turn, reaches ^{80}Kr through a series of (γ, n) reactions. For this reason, the increase of the ^{80}Kr abundance in the new model is not directly related to the adoption of the new ^{80}Kr neutron capture cross section as it occurs in low mass stars. On the contrary, it derives from the largely increased abundance of ^{87}Rb calculated using the new neutron capture cross section values. Even though a full GCE model is needed to fully validate our statement, we are confident that the use of our ^{80}Kr neutron capture cross section in stellar models will completely remove the current discrepancy between theory and solar observations. The new ^{84}Kr neutron capture cross section value leads to a decrease (-11%) of its yield in low-mass stars. Besides the minor variation of the neutron capture cross section at 30 keV between our measurement and [20], their trend at lower energies are different. The ^{84}Kr yield in the massive star model decreases by 9%. In those objects ^{84}Kr is produced by the C-shell burning at temperatures of the order of $\approx 1.5 \times 10^9$ K. In this temperature range, the new $^{84}\mathrm{Kr}(n,\gamma)^{85g}\mathrm{Kr}$ cross section is comparable to the reference one, while the new $^{84}\mathrm{Kr}(n,\gamma)^{85m}\mathrm{Kr}$ cross section is a factor of ≈ 2 larger than the reference. This favors the *s*-process branch through ^{85}Rb, justifying the reduction of ^{84}Kr. Another consequence of the adoption of new cross sections is also an increased yield from Sr to Zr (see below).

In an AGB star, the ^{85}Rb yield decreases by 5%, despite an enhanced neutron capture channel to the isomeric state of ^{85}Kr. This is a consequence of the concomitant action of neutron captures, β decays and mixing episodes during thermal pulses (TPs) in AGB stars. Those nuclear runaways are triggered by a sudden release of energy from the 3α process. When the temperature exceeds 270–280 MK, neutrons are provided from the $^{22}\mathrm{Ne}(\alpha,\mathrm{n})^{25}\mathrm{Mg}$ reaction. Those neutrons are easily captured by ^{85}Rb, but not from its unstable isobar ^{85}Kr, which has a lower neutron capture cross section (by about a factor of 4). Then, as the neutron burst ceases, the ^{85}Kr still alive in those layers decays to ^{85}Rb, replenishing its local abundance. The use of an enhanced neutron capture cross section to the isomer (which implies a lower ^{85}Kr ground state abundance) leads to a lower surface ^{85}Rb abundance. We hope that in the future experimental Rb isotopic ratios in presolar grains will be available in order to test the validity of these results. Another interesting result in our low mass model is that the combined effect of a weakened channel to the ground state of ^{85}Kr and, most importantly, of a slightly increased ^{86}Kr neutron capture cross section leads to a reduced yield for this isotope ($\approx -5\%$). As a consequence, the comparison to presolar grain data by [69] gets worse, and a larger production of ^{86}Kr is needed. Note that the same grain measurements would need a lower production for ^{80}Kr (in sharp contrast to the above described agreement with GCE calculations). It is important to stress that data published by [69] concern bulk measurements (i.e., not isolated single grains) and show large $^{84}\mathrm{Kr}/^{82}\mathrm{Kr}$ ratios with respect to any AGB model: they have been interpreted as a mix of pure *s*-process material coming from an AGB star and other solar system material which acted as contaminants. Moreover, we highlight that the abundances of both isotopes strongly depend on branching points (at ^{79}Se and ^{85}Kr, respectively). The neutron capture cross section of these two unstable nuclides has not been directly measured and will need future dedicated studies.

The use of the new cross section values leads, in massive stars, to an increased production of the two *s*-only isotopes ^{86}Sr and ^{87}Sr. The solar abundances of these two Sr isotopes receive an almost equal contribution from AGB stars and massive stars [6]. Thus, the increase by 31% and 13% of ^{86}Sr and ^{87}Sr yields in massive-star nucleosynthesis should in principle lead to a relative increase of, respectively, $\approx 15\%$ and 7% with the caveats already highlighted in the discussion of AGB stars. In massive stars, we also found an increased production of isotopes from ^{87}Rb (+47%) to ^{88}Sr and ^{90}Zr (both +7%).[1] The increase of ^{87}Rb obtained with the new cross section values is responsible also for the increase of ^{84}Sr in the massive-star model (+24%). The latter is produced during the O-shell burning by the following sequence of reactions $^{87}\mathrm{Rb}(\gamma,n)^{86}\mathrm{Rb}(\gamma,n)^{85}\mathrm{Rb}$ followed by $^{85}\mathrm{Rb}(p,n)^{85}\mathrm{Sr}(\gamma,n)^{84}\mathrm{Sr}$. Therefore, the abundance of ^{84}Sr directly scales with the abundance of ^{87}Rb. Another *p*-nuclide yield, ^{78}Kr, is increased (+7%) in the massive-star model, despite its new larger neutron capture cross section. This can be easily understood in terms of photodisintegration processes on the enhanced ^{80}Kr, which take place during the core Ne- and O-burning phases. More details will be provided in a dedicated paper.

VI. SUMMARY

The neutron capture cross sections of all Kr isotopes amenable to measurement by the activation technique were measured in the intense ≈ 40 keV quasi-Maxwellian neutron field of the SARAF-LiLiT facility. This study applies for the first time the technique of atom counting by atom trap trace analysis for the determination of a reaction nuclear cross section leading to long-lived products (^{81}Kr and ^{85g}Kr). The atom counting measurements were combined with decay counting by γ spectrometry for the short-lived Kr isotopes. The experimental cross sections were converted to Maxwell-averaged cross sections using the energy dependence of the JEFF-3.3 neutron library cross section. Significant differences in the measured capture cross section feeding two short-lived isotopes (^{79}Kr and ^{85m}Kr) are observed. Good agreement is obtained with the most recent cross section measurement by time of flight of Mutti *et al.* [20] for the cases measured in both studies. By comparison with reference calculations, we show that the new set of cross section values has a significant impact on *s*-process calculations of production of Kr isotopes and surrounding nuclides, in particular for massive-star nucleosynthesis involved in the weak *s* process.

ACKNOWLEDGMENTS

We would like to thank the SARAF and LiLiT (Soreq NRC) staffs for their dedicated help during the experiments. This work was supported in part by the Israel Science Foundation (Grant No. 1387/15), the Pazy Foundation (Israel), the German-Israeli Foundation (GIF No. I-1500-303.7/2019), and the U.S. Department of Energy, Office of Nuclear Physics, under Contract No. DE-AC02-06CH11357. This research has received funding from the European Research Council under the European Unions's Seventh Framework Program (FP/2007-2013), ERC Grant Agreement No. 615126.

---

[1] Note that the massive star model has been calculated with the lowest value [18] in the literature.

TABLE XIII. Weighted average cross sections (mb) of the ^{197}Au$(\gamma, n)^{196}$Au and ^{80,86}Kr$(\gamma, n)^{79,85m}$Kr reactions induced by 17.6 MeV (γ_0) and 14.6 MeV (γ_1) γ rays from the ^{7}Li$(p, \gamma)^8$Be reaction measured in this work and compared to literature.

Ref.	^{196}Au	^{79}Kr	^{85m}Kr
TENDL-2019 [70]	271	105	80.4
C. Plaisir *et al.* [71]	229(20)		
A. Veyssiere *et al.* [72]	285(10)		
This work	238(32)	67(10)	71(9)

APPENDIX: (γ, n) CROSS SECTIONS

Our data allow us to extract as a by-product of irradiation B the average cross section of the ^{197}Au$(\gamma, n)^{196}$Au and ^{80,86}Kr$(\gamma, n)^{79,85m}$Kr reactions induced by the 17.6 MeV (γ_0) and 14.6 MeV (γ_1) transitions from the ^{7}Li$(p, \gamma)^8$Be reaction. The ^{86}Kr$(\gamma, n)^{85}$Kr cross section cannot be retrieved from the data because of the dominant contribution of anthropogenic ^{85}Kr in the contemporary atmospheric Kr used in irradiation B. The γ-ray intensities are estimated by extrapolation of the data of [59] to the proton energy (1816 keV) in our measurements and the ratio (1.2) between the γ_1 and γ_0 transitions is taken from [59] as well. The experimental cross sections are compared in Table XIII to those calculated in the TENDL-2019 library [70] and to previous measurements for ^{197}Au$(\gamma, n)^{196}$Au. The ^{80,86}Kr$(\gamma, n)^{79,85m}$Kr reactions have not been investigated experimentally prior to our work.

[1] A. G. W. Cameron, Publ. Astron. Soc. Pac. **69**, 201 (1957).
[2] E. M. Burbidge, G. R. Burbidge, W. A. Fowler, and F. Hoyle, Rev. Mod. Phys. **29**, 547 (1957).
[3] F. Käppeler, Prog. Part. Nucl. Phys. **43**, 419 (1999).
[4] M. Pignatari, R. Gallino, M. Heil, M. Wiescher, F. Käppeler, F. Herwig, and S. Bisterzo, Astrophys. J. **710**, 1557 (2010).
[5] F. Käppeler, R. Gallino, S. Bisterzo, and W. Aoki, Rev. Mod. Phys. **83**, 157 (2011).
[6] N. Prantzos, C. Abia, S. Cristallo, M. Limongi, and A. Chieffi, Mon. Not. R. Astron. Soc. **491**, 1832 (2020).
[7] E. Anders and N. Grevesse, Geochim. Cosmochim. Acta **53**, 197 (1989).
[8] M. Asplund, N. Grevesse, A. J. Sauval, and P. Scott, Annu. Rev. Astron. Astrophys. **47**, 481 (2009).
[9] K. Lodders, H. Palme, and H.-P. Gail, 4.4 Abundances of the elements in the solar system, in *Solar System*, Datasheet from Landolt-Börnstein - Group VI Astronomy and Astrophysics Volume 4B, edited by J. Trümper (Springer-Verlag, Berlin, 2000).
[10] L. Alaerts, R. S. Lewis, J. Matsuda, and E. Anders, Geochim. Cosmochim. Acta **44**, 189 (1980).
[11] U. Ott, F. Begemann, J. Yang, and S. Epstein, Nature (London) **332**, 700 (1988).
[12] R. S. Lewis, S. Amari, and E. Anders, Geochim. Cosmochim. Acta **58**, 471 (1994).
[13] R. Gallino, M. Busso, G. Picchio, and C. M. Raiteri, Nature (London) **348**, 298 (1990).
[14] S. Raman, B. Fogelberg, J. A. Harvey, R. L. Macklin, P. H. Stelson, A. Schröder, and K. L. Kratz, Phys. Rev. C **28**, 602 (1983).
[15] G. Walter, B. Leugers, F. Käppeler, Z. Y. Bao, G. Reffo, and F. Fabbri, Nucl. Sci. Eng. **93**, 357 (1986).
[16] G. Walter, H. Beer, F. Käppeler, and R.-D. Penzhorn, Astron. Astrophys. **155**, 247 (1986).
[17] F. Käppeler, A. A. Naqvi, and M. Al-Ohali, Phys. Rev. C **35**, 936 (1987).
[18] H. Beer, Astrophys. J. **375**, 823 (1991).
[19] A. Tomyo, Y. Nagai, T. Shima, H. Makii, K. Mishima, M. Segawa, and M. Igashira, Nucl. Phys. A **718**, 530 (2003).
[20] P. Mutti, H. Beer, A. Brusegan, F. Corvi, and R. Gallino, in *International Conference on Nuclear Data for Science and Technology, 26 Sept.–1 Oct. 2004, Santa Fe,* edited by R. C. Haight, M. B. Chadwick, T. Kawano, and P. Talou, AIP Conf. Proc. 769 (AIP, New York, 2005), p. 1327.
[21] R. Raut, A. P. Tonchev, G. Rusev, W. Tornow, C. Iliadis, M. Lugaro, J. Buntain, S. Goriely, J. H. Kelley, R. Schwengner, A. Banu, and N. Tsoneva, Phys. Rev. Lett. **111**, 112501 (2013).
[22] I. Mardor, O. Aviv, M. Avrigeanu, D. Berkovits, A. Dahan, T. Dickel, I. Eliyahu, M. Gai, I. Gavish-Segev, S. Halfon, M. Hass, T. Hirsh, B. Kaiser, D. Kijel, A. Kreisel, Y. Mishnayot, I. Mukul, B. Ohayon, M. Paul, A. Perry *et al.*, Eur. Phys. J. A **54**, 91 (2018).
[23] M. Paul, M. Tessler, M. Friedman, S. Halfon, T. Palchan, L. Weissman, A. Arenshtam, D. Berkovits, Y. Eisen, I. Eliahu, G. Feinberg, D. Kijel, A. Kreisel, I. Mardor, G. Shimel, A. Shor, and I. Silverman, Eur. Phys. J. A **55**, 44 (2019).
[24] S. Halfon, A. Arenshtam, D. Kijel, M. Paul, D. Berkovits, I. Eliyahu, G. Feinberg, M. Friedman, N. Hazenshprung, I. Mardor, A. Nagler, G. Shimel, M. Tessler, and I. Silverman, Rev. Sci. Instrum. **84**, 123507 (2013).
[25] S. Halfon, A. Arenshtam, D. Kijel, M. Paul, L. Weissman, O. Aviv, D. Berkovits, O. Dudovitch, Y. Eisen, I. Eliyahu, G. Feinberg, G. Haquin, N. Hazenshprung, A. Kreisel, I. Mardor, G. Shimel, A. Shor, I. Silverman, M. Tessler, and Z. Yungrais, Rev. Sci. Instrum. **85**, 056105 (2014).
[26] M. Tessler, M. Paul, L. Weissman, J. Zappala, D. Baggenstos, S. Halfon, T. Heftrich, W. Jiang, A. Kreisel, Z. Lu, P. Mueller, R. Purtschert, R. Reifarth, A. Shor, D. Veltum, and M. Weigand, J. Phys.: Conf. Ser. **1668**, 012043 (2020).
[27] A. O. Hanson and D. L. Benedict, Phys. Rev. **65**, 33 (1944).
[28] R. Taschek and A. Hemmendinger, Phys. Rev. **74**, 373 (1948).
[29] H. Beer and F. Käppeler, Phys. Rev. C **21**, 534 (1980).
[30] W. Ratynski and F. Käppeler, Phys. Rev. C **37**, 595 (1988).
[31] A. Kreisel, L. Weissman, A. Arenshtam, Y. B. Aliz, D. Berkovits, Y. Buzaglo, O. Dudovich, Y. Eisen, I. Eliyahu, G. Feinberg, I. Fishman, I. Gertz, A. Grin, S. Halfon, Y. Haruvy, T. Hirsh, D. Hirschmann, Z. Horvitz, B. Kaizer, D. Kijel *et al.*, in *LINAC14: Proceedings of the 27th International Linear Accelerator Conference, Geneva, 2014* (CERN, Geneva, 2014), p. WEIOB02.
[32] G. Feinberg, M. Paul, A. Arenshtam, D. Berkovits, D. Kijel, A. Nagler, and I. Silverman, Nucl. Phys. A **827**, 590c (2009).

[33] G. Rupp, D. Petrich, F. Käppeler, J. Kaltenbaek, B. Leugers, and R. Reifarth, Nucl. Instrum. Methods Phys. Res., Sect. A **608**, 152 (2009).

[34] L. Weissman, D. Berkovits, A. Arenshtam, Y. Ben-Aliz, Y. Buzaglo, O. Dudovitch, Y. Eisen, I. Eliyahu, G. Feinberg, I. Fishman, I. Gertz, A. Grin, S. Halfon, D. Har-Even, Y. Haruvy, D. Hirschmann, T. Hirsh, Z. Horovitz, B. Kaizer, D. Kijel *et al.*, J. Instrum. **10**, T10004 (2015).

[35] G. Feinberg, Study of the ^{7}Li(p, n) reaction towards measurements of neutron-capture cross sections in the astrophysical *s*-process with the SARAF accelerator and a liquid-lithium target, Ph.D. thesis, The Hebrew University of Jerusalem, 2014 (unpublished), available online: http://arad.mscc.huji.ac.il/dissertations/W/JSL/001975970.pdf.

[36] H. Loosli and H. Oeschger, Earth Planet. Sci. Lett. **7**, 67 (1969).

[37] A. Turkevich, L. Winsberg, H. Flotow, and R. M. Adams, Proc. Natl. Acad. Sci. USA **94**, 7807 (1997).

[38] M. Tessler, M. Paul, A. Arenshtam, G. Feinberg, M. Friedman, S. Halfon, D. Kijel, L. Weissman, O. Aviv, D. Berkovits, Y. Eisen, I. Eliyahu, G. Haquin, A. Kreisel, I. Mardor, G. Shimel, A. Shor, I. Silverman, and Z. Yungrais, Phys. Lett. B **751**, 418 (2015).

[39] J. Zappala, D. Baggenstos, C. Gerber, W. Jiang, B. Kennedy, Z.-T. Lu, J. Masarik, P. Mueller, R. Purtschert, and A. Visser, Geophys. Res. Lett. **47**, e2019GL086381 (2020).

[40] M. Friedman, D. Cohen, M. Paul, D. Berkovits, Y. Eisen, G. Feinberg, G. Giorginis, S. Halfon, A. Krsa, A. Plompen, and A. Shor, Nucl. Instrum. Methods Phys. Res., Sect. A **698**, 117 (2013).

[41] S. Agostinelli, J. Allison, K. Amako, J. Apostolakis, H. Araujo, P. Arce, M. Asai, D. Axen, S. Banerjee, G. Barrand, F. Behner, L. Bellagamba, J. Boudreau, L. Broglia, A. Brunengo, H. Burkhardt, S. Chauvie, J. Chuma, R. Chytracek, G. Cooperman *et al.*, Nucl. Instrum. Methods Phys. Res., Sect. A **506**, 250 (2003), version GEANT4.10.03.p03.

[42] G. Feinberg, M. Friedman, A. Krása, A. Shor, Y. Eisen, D. Berkovits, D. Cohen, G. Giorginis, T. Hirsh, M. Paul, A. J. M. Plompen, and E. Tsuk, Phys. Rev. C **85**, 055810 (2012).

[43] D. Brown, M. Chadwick, R. Capote, A. Kahler, A. Trkov, M. Herman, A. Sonzogni, Y. Danon, A. Carlson, M. Dunn, D. Smith, G. Hale, G. Arbanas, R. Arcilla, C. Bates, B. Beck, B. Becker, F. Brown, R. Casperson, J. Conlin *et al.*, Nucl. Data Sheets **148**, 1 (2018).

[44] C. Lederer *et al.* (n_TOF Collaboration), Phys. Rev. C **83**, 034608 (2011).

[45] C. Massimi, B. Becker, E. Dupont, S. Kopecky, C. Lampoudis, R. Massarczyk, M. Moxon, V. Pronyaev, P. Schillebeeckx, I. Sirakov, and R. Wynants, Eur. Phys. J. A **50**, 124 (2014).

[46] H. Xiaolong, Nucl. Data Sheets **110**, 2533 (2009).

[47] B. Singh, Nucl. Data Sheets **96**, 1 (2002).

[48] C. M. Baglin, Nucl. Data Sheets **109**, 2257 (2008).

[49] B. Singh and J. Chen, Nucl. Data Sheets **116**, 1 (2014).

[50] R. Helmer, Nucl. Data Sheets **95**, 543 (2002).

[51] C. Chen, Y. Li, K. Bailey, T. O'Connor, L. Young, and Z.-T. Lu, Science **286**, 1139 (1999).

[52] W. Jiang, K. Bailey, Z.-T. Lu, P. Mueller, T. P. O'Connor, C.-F. Cheng, S.-M. Hu, R. Purtschert, N. Sturchio, Y. Sun, W. Williams, and G.-M. Yang, Geochim. Cosmochim. Acta **91**, 1 (2012).

[53] W. Jiang, K. Bailey, Z.-T. Lu, P. Mueller, T. O'Connor, and R. Purtschert, Opt. Lett. **39**, 409 (2014).

[54] J. Zappala, D. McLain, P. Mueller, and J. Steeb, J. Radioanal. Nucl. Ch. **326**, 1075 (2020).

[55] J. C. Zappala, K. Bailey, P. Mueller, T. P. O'Connor, and R. Purtschert, Water Resour. Res. **53**, 2553 (2017).

[56] C. Schlosser, A. Bollhöfer, S. Schmid, R. Krais, J. Bieringer, and M. Konrad, Appl. Radiat. Isot. **126**, 16 (2017).

[57] H. Loosli and R. Purtschert, in *Isotopes in the Water Cycle: Past, Present and Future of a Developing Science*, edited by P. K. Aggarwal, J. R. Gat, and K. F. Froehlich (Springer Netherlands, Dordrecht, 2005), pp. 91–96.

[58] R. Purtschert, R. Yokochi, and N. Sturchio, in *Isotope Methods for Dating Old Groundwater*, edited by A. Suckow, P. Aggarwal, and L. Araguas-Araguas (IAEA, Vienna, 2013), Chap. 5, pp. 91–124.

[59] D. Zahnow, C. Angulo, C. Rolfs, S. Schmidt, W. Schulte, and E. Somorjai, Z. Phys.: Hadrons Nucl. **351**, 229 (1995).

[60] M. Tessler, M. Paul, S. Halfon, B. S. Meyer, R. Pardo, R. Purtschert, K. E. Rehm, R. Scott, M. Weigand, L. Weissman, S. Almaraz-Calderon, M. L. Avila, D. Baggenstos, P. Collon, N. Hazenshprung, Y. Kashiv, D. Kijel, A. Kreisel, R. Reifarth, D. Santiago-Gonzalez *et al.*, Phys. Rev. Lett. **121**, 112701 (2018).

[61] JEFF-3.3, Joint Evaluated Fission and Fusion database, 2017, https://www.oecd-nea.org/dbdata/jeff/jeff33/index.html.

[62] I. Dillmann, R. Plag, F. Käppeler, and T. Rauscher, in *EFNUDAT Fast Neutrons - Scientific Workshop on Neutron Measurements, Theory & Applications* (JRC-IRMM, Geel, Belgium, 2009).

[63] D. Vescovi, S. Cristallo, M. Busso, and N. Liu, Astrophys. J. Lett. **897**, L25 (2020).

[64] L. Roberti *et al.* (unpublished).

[65] R. Gallino, C. Arlandini, M. Busso, M. Lugaro, C. Travaglio, O. Straniero, A. Chieffi, and M. Limongi, Astrophys. J. **497**, 388 (1998).

[66] O. Straniero, R. Gallino, and S. Cristallo, Nucl. Phys. A **777**, 311 (2006).

[67] A. Chieffi and M. Limongi, Astrophys. J. **764**, 21 (2013).

[68] S. Cristallo, C. Abia, O. Straniero, and L. Piersanti, Astrophys. J. **801**, 53 (2015).

[69] R. S. Lewis, S. Amari, and E. Anders, Nature (London) **348**, 293 (1990).

[70] A. Koning, D. Rochman, J.-Ch. Sublet, N. Dzysiuk, M. Fleming, and S. der Marck, Nucl. Data Sheets **155**, 1 (2019).

[71] C. Plaisir, F. Hannachi, F. Gobet, M. Tarisien, M. Aleonard, V. Meot, G. Gosselin, P. Morel, and B. Morillon, Eur. Phys. J. A **48**, 68 (2012).

[72] A. Veyssiere, H. Beil, R. Bergere, P. Carlos, and A. Lepretre, Nucl. Phys. A **159**, 561 (1970).